

## Does CO<sub>2</sub> Permeate through Aquaporin-1?

Jochen S. Hub and Bert L. de Groot

Computational Biomolecular Dynamics Group, Max-Planck-Institute for Biophysical Chemistry, Göttingen, Germany

**ABSTRACT** Aquaporins facilitate water permeation across biological membranes. Additionally, glycerol and other small neutral solutes are permeated by related aquaglyceroporins. The role of aquaporins in gas permeation has been a long-standing and controversially discussed issue. We present an extensive set of atomistic molecular dynamics simulations that address the question of CO<sub>2</sub> permeation through human aquaporin-1. Free energy profiles derived from the simulations display a barrier of ~23 kJ/mol in the aromatic/arginine constriction region of the water pore, whereas a barrier of ~4 kJ/mol was observed for a palmitoyloleoylphosphatidylethanolamine lipid bilayer membrane. The results indicate that significant aquaporin-1-mediated CO<sub>2</sub> permeation is to be expected only in membranes with a low intrinsic CO<sub>2</sub> permeability.

### INTRODUCTION

Aquaporins are passive integral membrane channels facilitating efficient, yet selective permeation of water across biological membranes (1,2). Also, glycerol and other small linear alcohols are known to permeate via related aquaglyceroporins like GlpF from *Escherichia Coli* (3). So far, thirteen different aquaporins and aquaglyceroporins with different specificities have been identified in humans. They are expressed in tissues as diverse as the kidney, lung, red blood cells, brain, and the eye lens. Malfunction of aquaporins has been shown to be associated with a number of pathological conditions (4–8). The elucidation of the structure of different aquaporins (9–13) and aquaglyceroporins (14,15) formed the basis for the determination of the molecular mechanism of water permeation and proton exclusion by molecular dynamics simulations (16–21).

It has been a long-standing and controversially discussed question whether also gas transport across biological membranes is facilitated by aquaporins, or whether gases like carbon dioxide can freely permeate lipid bilayer membranes. The role of aquaporin-1 (AQP1) for CO<sub>2</sub> permeation in mammalian lungs and red blood cells, for example, remains unclear (22–29). Part of the controversy is apparently due to the fact that i), CO<sub>2</sub> permeation is usually measured indirectly, via acidification through the action of carbonic anhydrase (CA); ii), that, depending on the pH and on the concentration of CA, the CO<sub>2</sub> permeation is limited by unstirred water layers on both sides of the membrane (30); iii), that in erythrocytes this acidification is additionally influenced by the action of the HCO<sub>3</sub><sup>-</sup>-Cl<sup>-</sup> transporter; and that iv), inhibitors like 4,4'-diisothiocyanato-stilbene-2,2'-disulfonic acid (DIDS) and mercurial compounds may not be specific for the HCO<sub>3</sub><sup>-</sup>-Cl<sup>-</sup> transporter and AQP1, respectively (26–29). Moreover, there is a large variability in the CO<sub>2</sub> permeability of different membranes (26,29–31).

Another process for which aquaporin-mediated CO<sub>2</sub> permeation has been suggested to play a physiological role is photosynthesis. In a recent study it was shown that the leaf growth of tobacco plants was dependent on the level of NtAQP1 expression, an aquaporin homologous to human AQP1 (32).

Here, we study the barrier for CO<sub>2</sub> permeation through AQP1 as well as through a pure palmitoyloleoylphosphatidylethanolamine (POPE) bilayer, using extensive atomistic molecular dynamics simulations. We address the question whether CO<sub>2</sub> is likely to permeate through AQP1 and close homologs like the plant aquaporin NtAQP1 by comparing the free energy for CO<sub>2</sub> permeation through AQP1 to the corresponding profiles for a model lipid bilayer membrane. Moreover, we present profiles for CO<sub>2</sub> interactions along possible permeation pathways and estimate permeation coefficients.

### METHODS

An equilibrated simulation box of a tetramer of human AQP1 embedded in a solvated lipid bilayer was chosen as starting configuration of the simulations. The starting structure of human AQP1 was modeled based on the x-ray structure of bovine AQP1 (PDB code 1J4N (10)) by mutating differing residues using the WHAT IF modeling software (33). The two sequences are 91% sequence identical, making a structural overlay straightforward. The periodic simulation box contained the AQP1 tetramer, 271 POPE lipids and 19769 TIP4P (34) water molecules. The OPLS all-atom force field (35,36) was employed for the protein, lipid parameters were taken from Berger et al. (37). Four chloride ions were added to neutralize the simulation cell. The system was equilibrated for 2 ns before the production simulations. A typical simulation box is shown in Fig. 1 *a*.

All simulations were carried out using the GROMACS simulation software (38,39). Electrostatic interactions were calculated with the particle-mesh Ewald method (40,41). Short-range repulsive and attractive dispersion interactions were described together by a Lennard-Jones potential, which was cut off at 1.0 nm. The Settle (42) algorithm was used to constrain bond lengths and angles of water molecules, and LINCS (43) was used to constrain all other bond lengths, allowing a time step of 2 fs. The simulation temperature was kept constant by weakly ( $\tau = 0.1$  ps) coupling the protein, lipids, and solvent separately to a temperature bath (44) of 300 K. Likewise, the pressure was kept constant by weakly coupling the system to a pressure bath of 1 bar. The *xy* (membrane plane) direction was pressure coupled with

Submitted January 16, 2006, and accepted for publication April 27, 2006.

Address reprint requests to Bert L. de Groot, Tel.: 49-551-201-2308; Fax: 49-551-201-2302; E-mail: bgroot@gwdg.de.

© 2006 by the Biophysical Society

0006-3495/06/08/842/07 \$2.00

doi: 10.1529/biophysj.106.081406

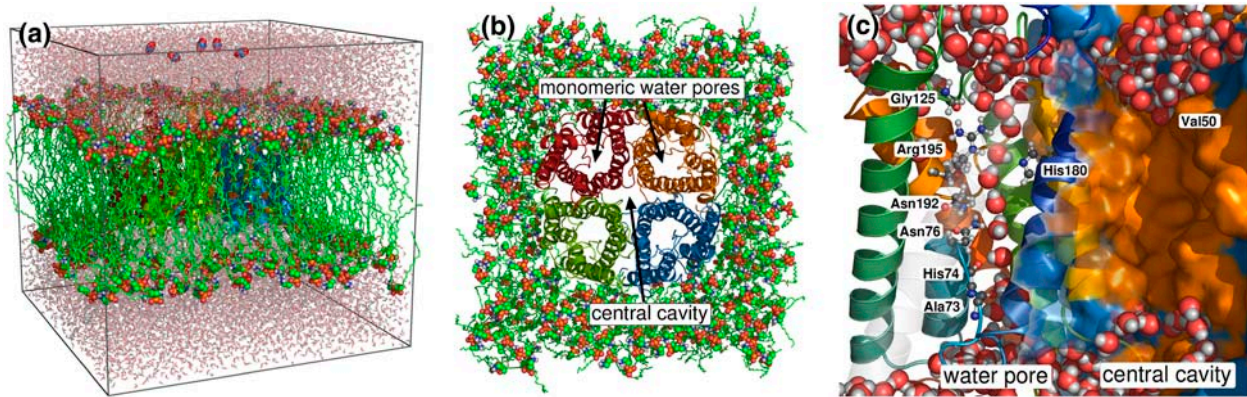


FIGURE 1 (a) Typical simulation setup of an AQP1 tetramer, solvated in a POPE bilayer and water. Five CO<sub>2</sub> molecules in bulk water are shown in blue and red. (b) In the top view, the four monomeric water pores and the central cavity can be identified. (c) A snapshot taken from an equilibrium simulation showing a water pore (helices and ribbon representation) filled by a single file of water, and the central cavity along the fourfold axis of the tetramer (surface representation). The surface representation is colored according to residue hydrophobicity: hydrophobic residues in orange, hydrophilic residues in blue. All figures with molecular representations were made with PyMOL (50).

a coupling constant  $\tau$  of 1 ps, whereas the box length in  $z$ -direction was kept fixed to avoid artifacts in the umbrella sampling simulations (see below).

The CO<sub>2</sub> simulations were set up as follows: the AQP1 channel was divided into 0.5-Å wide equidistant sections with the center of each section representing an umbrella center. For each section the equilibrated trajectory was searched for snapshots with water molecules as close as possible to the chosen position of the umbrella potential. This water molecule was subsequently replaced by CO<sub>2</sub>. Umbrella sampling calculations were carried out by applying a harmonic restraint force along the pore coordinate with force constants between 100 and 6400 kJ/mol/nm<sup>2</sup>. The umbrella sampling simulations were performed with CO<sub>2</sub> with the restraint acting on the carbon atom, and—for comparison and to validate the procedure—with water by restraining the oxygen atom. No restraint along the lateral directions was applied.

We observed that a possible flexibility of Arg-195 has strong impact on the barrier in the aromatic/arginine (ar/R) constriction region (see Results). Since these flexibilities are sampled slowly in the simulations we performed additional umbrella samplings in the ar/R region with starting positions taken from an independent equilibrium run. This way, eight independent channels contributed to our profile. Additionally, the protonation state of His-180 opposing the Arg-195 might influence the barrier height. In six out of eight channels simulated the  $\delta$ -nitrogen was protonated, in two channels the  $\epsilon^2$ -nitrogen. In accordance with a recent finding for water permeation, no significant influence of the protonation state of His-180 on the CO<sub>2</sub> barrier was found (45).

To reduce CPU time, and hence improve sampling, CO<sub>2</sub> molecules were placed in each pore and, to further improve statistics, at three or four positions along the channel coordinate within one simulation run. A minimal distance of 25 Å between CO<sub>2</sub> molecules along the pore was imposed to ensure that interactions between CO<sub>2</sub> molecules (if any) are negligibly small. The umbrella sampling histograms from all monomeric channels were combined to compute a free energy profile using the weighted histogram analysis method (WHAM) (46). To account for the periodicity of the system, we implemented a cyclic version of the WHAM procedure. In total, 3912 histograms from 400 ps simulations were obtained (taking only the last 300 ps for analysis and using the first 100 ps for equilibration), extracted from a total of 334 ns of simulation time of the aquaporin system.

Additionally, CO<sub>2</sub> molecules were placed along the central channel surrounding the tetrameric axis. Umbrella positions were chosen as before, either by replacing a water molecule, or by adding it to the structure in case of an empty position. For the central pore along the tetrameric axis, 888 histograms were obtained.

Umbrella simulations to obtain a free energy profile for water along the AQP1 pore were performed the same way, except that water molecules close to the desired minimum of the artificial potential were not replaced but were

directly restrained. Like for CO<sub>2</sub>, the individual umbrella simulations were carried out for 400 ps. In total, 3092 histograms were obtained. Force constants were chosen between 100 and 1600 kJ/mol/nm<sup>2</sup>.

Umbrella simulations for the lipid bilayer were performed by inserting CO<sub>2</sub> molecules at various positions into random snapshots of a 20-ns equilibrium run of a bilayer patch of 128 POPE and 4777 TIP4P water molecules. Up to 12 CO<sub>2</sub> molecules were inserted into one simulation keeping a minimum distance of 25 Å in the lateral direction and 30 Å perpendicular to the bilayer. A total of 3200 histograms were extracted from 260 simulations of 500 ps each, using the last 300 ps for analysis and the first 200 ps for equilibration. Force constants between 100 and 800 kJ/mol/nm<sup>2</sup> were used.

To account for fluctuations of each of the channels within the tetramer, the umbrella positions were corrected with respect to the center of the corresponding monomer. As a robust measure for the monomer position we chose the center of mass of the backbone atoms of the transmembrane helices.

Partial charges for CO<sub>2</sub> were obtained from electrostatic fitting using the CHELPG procedure to wavefunctions obtained at the RHF/6-31G\* level, resulting in a charge of 0.9378 $e$  on the carbon atom and  $-0.4689e$  on the oxygen atoms. The Lennard-Jones parameters  $\sigma$  and  $\epsilon$  for the CO<sub>2</sub> carbon were 0.375 nm and 0.439 kJ/mol, respectively, and for the CO<sub>2</sub> oxygen 0.296 nm and 0.877 kJ/mol, respectively. The CO<sub>2</sub> parameters were validated by comparison to the oil/water partition coefficient of CO<sub>2</sub>. The experimentally determined value of near unity (47) compares favorably to the small free energy difference for CO<sub>2</sub> between the bulk water phase and the lipid tail region of the bilayer (cf. Fig. 2, shaded curve).

Profiles for enthalpic interactions of CO<sub>2</sub> (Fig. 3) were calculated as the sum of short-range Coulomb interactions ( $\leq 1$  nm) and Lennard-Jones interactions. Note that these do not correspond to the total enthalpy for a given CO<sub>2</sub> position since they only include interactions directly involving CO<sub>2</sub>. CO<sub>2</sub>-induced alterations in the surroundings (like protein-water interactions) are not included in this component of the enthalpy. The profiles do, however, give more insight into the origin of the free energy barriers.

Permeability coefficients  $P_f$  for the POPE membrane were estimated by counting barrier crossings in simulations where CO<sub>2</sub> molecules were allowed to diffuse freely through a POPE bilayer (see below). After equilibration, we observed 3.4 barrier crossings per barrier, direction, and nanosecond. The permeability coefficient for one barrier of  $\Delta G^{\text{POPE}} = 4$  kJ/mol was calculated by  $P_f^{(1)} = \Phi / (S c_s)$  where  $\Phi = 3.4/\text{ns}$  denotes the transition rate,  $S = 30 \text{ nm}^2$  our membrane surface and  $c_s = 0.52 \text{ M}$  the CO<sub>2</sub> concentration, giving  $P_f^{(1)} = 23 \text{ cm}^2/\text{s}$ . Since half of the CO<sub>2</sub> molecules crossing the first barrier will return and not permeate through the bilayer this refers to an estimated permeability coefficient for POPE of  $P_f^{\text{POPE}} = 12 \text{ cm}^2/\text{s}$ .

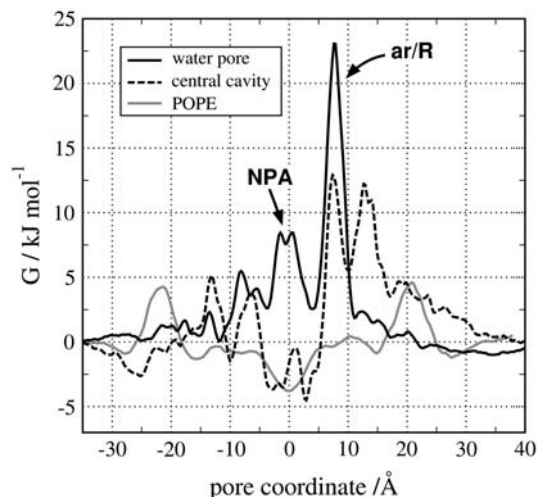


FIGURE 2 Free energy profile for CO<sub>2</sub> permeation through the aquaporin-1 water pore (black, solid line), the tetrameric central cavity (black, dashed line), and a POPE bilayer (shaded).

Using the permeability coefficient for a single POPE barrier we estimated the coefficients for the water pore and the central cavity via  $P_f = P_f^{(1)} \exp(-(\Delta G' - \Delta G^{\text{POPE}})/kT)$ . Here,  $\Delta G'$  denotes the barrier of the water pore or the central cavity,  $T$  the temperature, and  $k$  the Boltzmann constant. In terms of rate theory, this estimate assumes the same prefactor for CO<sub>2</sub> permeation across a single POPE barrier as through a channel. Additionally, it rests on the assumption that the permeation rate is limited solely by the main barrier along the reactive coordinate. Along the central cavity two barriers of the same height are present, giving rise to an additional factor of 1/2. Unit permeability coefficients were calculated by  $p_f = P_f S_{\text{mono}}$  since the free energy barriers were normalized to an area of one AQP monomer. We estimated the area of one monomer as  $S_{\text{mono}} = 10.3 \text{ nm}^2$ . Note that the area per monomer in vivo can be expected to be lower than the area per monomer in AQP1 crystals ( $11.5 \text{ nm}^2$ ) (48).

Statistical errors of the free energy profiles were estimated using bootstrap analysis. To account properly for limited long-time sampling, we performed bootstrap analysis by considering complete histograms as independent data points: From the  $N$  original histograms we randomly selected  $N$  histograms (allowing duplication) which were subsequently used for WHAM analysis. This procedure was performed 50 times for each profile allowing the calculation of standard deviations. The standard deviations at the main barriers were 1 kJ/mol for the monomeric channel, 2 kJ/mol for the central cavity, and 1 kJ/mol for the POPE membrane.

The barrier at the ar/R region in the monomeric channel is influenced strongly by the flexibility of Arg-195, which is sampled slowly (see above). Therefore, we calculated the barrier for each of the eight simulated channels separately. Considering these eight barriers as independent data points gave an additional uncertainty of 3 kJ/mol.

### Bulk water correction

Umbrella simulations such as presented here, with a molecule restrained to a certain  $z$ -position, i.e., to an  $x$ - $y$ -plane parallel to the bilayer, will not sample all possible  $x$ - $y$  positions in the simulated time window, especially within the bulk water region. This leads to an overestimation of the free energy level in the bulk region. The correction for this entropic effect is straightforward, as the effect is related to the sampled area (and hence, the simulation time). We therefore took advantage of the fact that in AQP1 the relative free energy for water can be obtained not only by umbrella simulations but also from the water number density distribution via  $G(z) = -kT \ln \rho(z)$ . The bulk free energy level for water can be easily and accurately determined from such a profile. A 14-ns equilibrium MD simulation was used for this purpose.

The bulk level was normalized to the area of an AQP1 monomer, estimated as approximately  $A_{\text{mono}} = 10.3 \text{ nm}^2$ , to allow direct comparison to the lipid membrane profile, which is independent on the area. The two profiles derived from the umbrella sampling simulations and from the water density distribution were found to be rather similar (Fig. 4), rendering an overlay of the two profiles straightforward. The resulting bulk level correction for the umbrella sampling simulations of water of  $\Delta G_{\text{w}}^{\text{bulk}} = 3.2 \text{ kJ/mol}$  was found to be relatively small. The correction is already incorporated in Fig. 4 as a linear trapezoidal correction to the umbrella profile in the pore entrance and exit region.

The bulk correction depends on the sampled area within the simulation which is approximately proportional to the diffusion constant of the solute. From simulations of a box of pure TIP4P water and of 20 CO<sub>2</sub> molecules solvated in 4084 TIP4P water molecules we calculated the diffusion constants of water and CO<sub>2</sub> in the simulations to  $D_{\text{w}} = 3.6 \times 10^{-5} \text{ cm}^2/\text{s}$  and  $D_{\text{CO}_2} = 2.7 \times 10^{-5} \text{ cm}^2/\text{s}$ , respectively, giving a bulk correction for CO<sub>2</sub> of  $\Delta G_{\text{CO}_2}^{\text{bulk}} = \Delta G_{\text{w}}^{\text{bulk}} + kT \ln(D_{\text{w}}/D_{\text{CO}_2}) = 3.9 \text{ kJ/mol}$ .

## RESULTS AND DISCUSSION

Fig. 2 shows the free energy profile obtained as a potential of mean force from a set of umbrella sampling simulations for three potential pathways for CO<sub>2</sub> permeation through AQP1 embedded in a lipid bilayer: the pathway through an aquaporin water pore (black, solid line), the central channel (black, dashed line), and through the POPE membrane (shaded line). In the monomeric water channel CO<sub>2</sub> molecules encounter a major barrier of  $\sim 23 \pm 4 \text{ kJ/mol}$  in the ar/R constriction region (also termed selectivity filter, see Fig. 1 c) and a lower one of  $\sim 9 \pm 1 \text{ kJ/mol}$  around the region with the two conserved NPA motifs. The corresponding enthalpic interactions of CO<sub>2</sub> to water and to the protein, respectively, are shown in Fig. 3 b. As can be seen, there is no significant loss of interactions involving CO<sub>2</sub> in the ar/R region, rendering the free energy barrier either entropic in nature, or, more likely, due to indirect enthalpic effects like an unfavorable configuration of surrounding water molecules. This is illustrated in Fig. 5, which shows a typical pathway of CO<sub>2</sub> through the monomeric AQP1 channel, as derived from the umbrella sampling simulations. As can be seen, water molecules form strong hydrogen bonds to Arg-195 in the ar/R region, which are broken upon CO<sub>2</sub> passage. Fig. 3 a shows 115 pathways for CO<sub>2</sub> molecules that were not restrained by an umbrella potential. The trajectories show that the CO<sub>2</sub> molecules behave as expected from the potential of mean force, not spontaneously passing the ar/R constriction region within the simulated time of 500 ps.

The barrier in the ar/R is strongly influenced by the flexibility of Arg-195. In the crystal structure, its guanidinium group points straight into the pore creating the narrowest part of the channel. Two water molecules forming H-bonds to the  $\epsilon$ - and  $\eta^1$ -nitrogens are displaced by a permeating CO<sub>2</sub> molecule (compare Fig. 5, *second* and *third picture* from *bottom*). In this configuration, the barrier is likely to be higher than 23 kJ/mol. However, during simulation we observed some flexibility of Arg-195 probably caused by flexibility in Loop C. Arg-195 is stabilized sterically by the neighboring Asn-127 and by a frequent

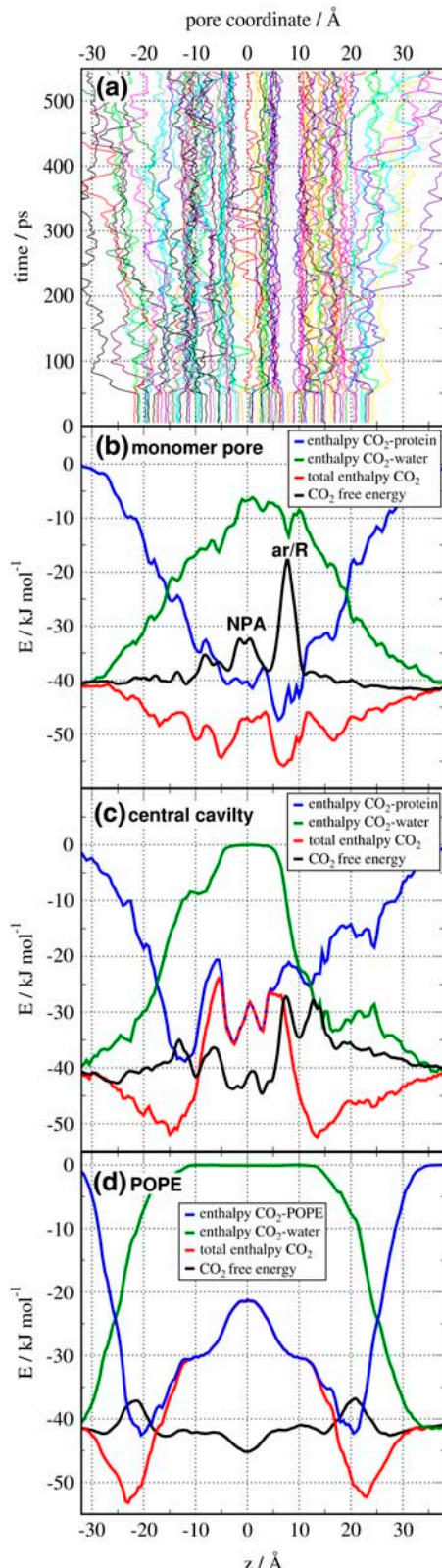


FIGURE 3 Trajectories of unrestrained CO<sub>2</sub> molecules in the monomeric AQP1 channel (a), and profiles of enthalpic interactions of CO<sub>2</sub> with water (green), protein or POPE, respectively (blue), and total (red) together with the free energy profiles of (cf. Fig. 2, black) for the monomeric channel (b),

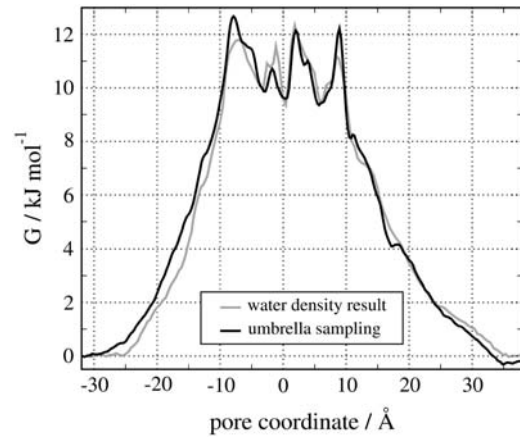


FIGURE 4 Free energy profiles of water through the monomeric AQP1 pore obtained by umbrella simulations (solid) and from evaluation of the water density distribution (shaded).

H-bond to the carbonyl oxygen of Gly-125 (see Fig. 1). In such cases, no breakage of H-bonds between water and Arg-195 is necessary lowering the barrier for CO<sub>2</sub> passage significantly. The effect of the flexibility of Arg-195 on the CO<sub>2</sub> barrier is reflected by the reported uncertainty of 4 kJ/mol.

As described in the methods section we roughly estimated the unit permeability coefficient for CO<sub>2</sub> permeation through AQP1 to be  $p_f = 1 \times 10^{-15} \text{ cm}^3/\text{s}$ . The error of 4 kJ/mol in the main barrier corresponds to factor of 5 in the permeabilities, i.e., a range of  $2 \times 10^{-16}$  to  $5 \times 10^{-15}$ . The unit permeability coefficient for water permeation through a two-dimensional AQP1 crystal is  $p_f^{\text{water}} = 5.43 \times 10^{-14} \text{ cm}^3/\text{s}$  (48), thus, the resistance of AQP1 to CO<sub>2</sub> is between one and two orders of magnitude higher in comparison to water. This result can also be expected by comparison of the corresponding free energy barriers of 12 and 23 kJ/mol, respectively.

The single channel permeability estimated from our results can be compared with the results from Nakhoul et al. (22), Prasad et al. (24), and Yang et al. (25) from experiments with oocytes, erythrocytes, and proteoliposomes containing AQP1. As discussed by Yang et al. (25), the results reported by Nakhoul et al. (22) refer to a single channel CO<sub>2</sub> permeability of  $1\text{--}2 \times 10^{-14} \text{ cm}^3/\text{s}$ , whereas the results reported by Prasad et al. (24) give  $\sim 5 \times 10^{-15} \text{ cm}^3/\text{s}$ . Yang et al. (25) did not observe AQP1-mediated CO<sub>2</sub> permeation and reported an upper limit of  $3 \times 10^{-16} \text{ cm}^3/\text{s}$ . Therefore, our estimate of  $\sim 1 \times 10^{-15} \text{ cm}^3/\text{s}$  most closely matches the result by Prasad et al. and the upper limit by Yang et al.

A second possible pathway through AQP1 would be the central pore along the fourfold axis of the tetramer. Due to its hydrophobicity the central pore is neither filled by water nor does it conducts water (see Fig. 1 c). Two major barriers for

the central channel around the tetramer axis (c), and through the POPE bilayer (d). The enthalpic profiles only show interactions involving CO<sub>2</sub> and do not contain interactions within the CO<sub>2</sub>'s surroundings.

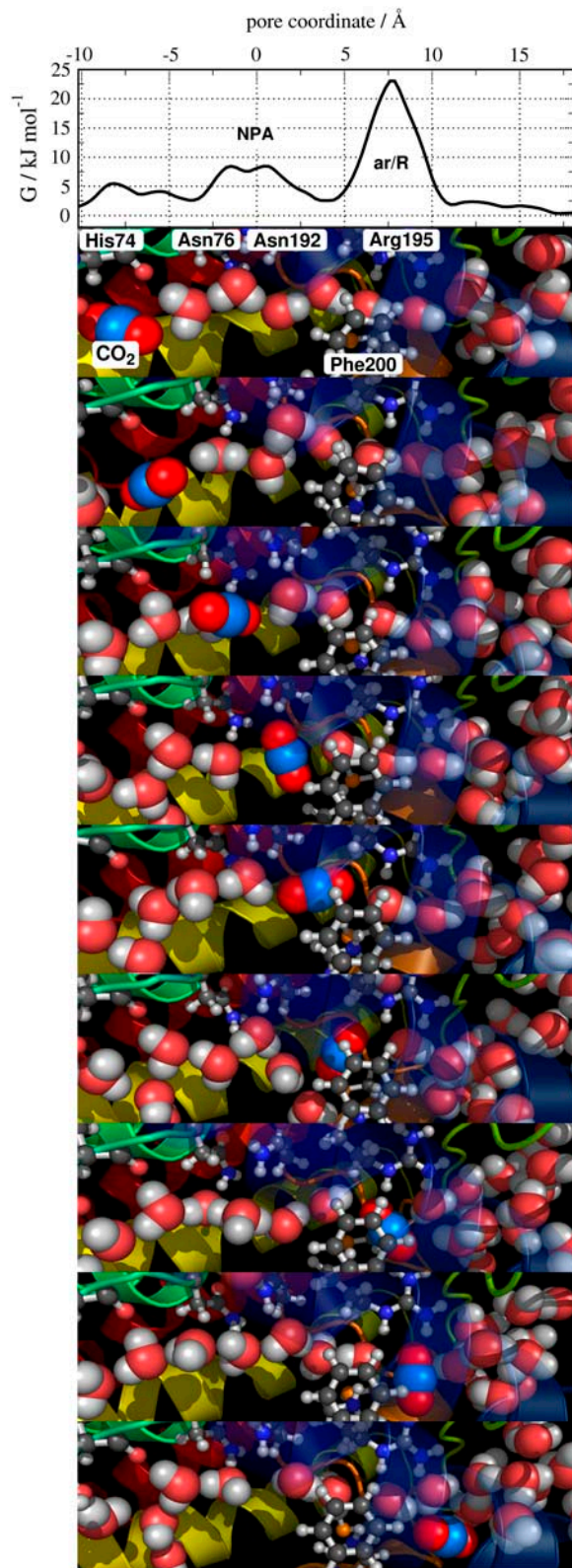


FIGURE 5 A CO<sub>2</sub> at various positions along the water channel indicating a possible pathway for CO<sub>2</sub> along the NPA motifs and through the aromatic/arginine constriction region. The CO<sub>2</sub> molecule is colored in red and marine blue. On top of the sequence, the corresponding free energy is plotted, indicating the 23 kJ/mol barrier putatively caused by competition for

CO<sub>2</sub> permeation can be identified: first, a barrier of  $\sim 12 \pm 2$  kJ/mol at  $z = 7.5$  Å is located near the extracellular entrance to the central cavity, surrounded by the 4 Val-50 of the 4 monomers. In this region CO<sub>2</sub> molecules lose favorable interactions to neighboring water molecules (compare Fig. 3 *c*, green and red lines). A second barrier of the same height is found  $\sim 7$  Å above the first one. Here, the CO<sub>2</sub> is surrounded by the 4 Asp-48, and hence, it is likely that CO<sub>2</sub> competes with water for hydrogen bonds to Asp-48. The barrier translates into a permeability coefficient of  $P_f = 0.1$  cm/s for the central cavity, referring to the area of an AQP1 tetramer, or a unit permeability coefficient of  $p_f = 4 \times 10^{-14}$  cm<sup>3</sup>/s.

The free energy barrier for CO<sub>2</sub> permeation through the central cavity is significantly smaller than for the monomeric channel. When taking into account that each tetramer contributes four monomeric channels and one central pore, these barriers would imply that  $\sim 10\%$  of AQP1-permeated CO<sub>2</sub> would be expected to permeate via the monomeric channels. Note, however, that in these calculations we have assumed an empty central channel. Should an ion or organic molecule be bound in the central cavity under physiological conditions (like in the recently resolved structure of an aquaporin-Z tetramer (49)), this would be expected to drastically increase the barrier for CO<sub>2</sub> permeation through the central pore. Experiments with mercurial AQP1 blockers and with the C189S mutant suggest that AQP1-mediated CO<sub>2</sub> permeation takes place through the monomeric pore (23,24), which would imply that, indeed, the central channel is blocked under the experimental conditions.

The tobacco aquaporin NtAQP1 was recently reported to facilitate physiologically relevant CO<sub>2</sub> permeation (32). The pore region of NtAQP1 is highly similar to human AQP1, with the residues surrounding the major barriers in the NPA and ar/R region fully conserved among the two proteins (32). Our results suggest that—if the central channel is blocked—aquaporin-mediated CO<sub>2</sub> permeation is expected to play a significant role in photosynthesis only if the plant cell membranes have a low intrinsic CO<sub>2</sub> permeability, with an activation barrier well above 20 kJ/mol. However, since the structure of the central pore of NtAQP1 is unknown, we cannot exclude that permeation via the central pore lowers the effective barrier.

### Membrane permeability

To address the physiological significance of CO<sub>2</sub> permeation through AQP1, we calculated the free energy barrier for CO<sub>2</sub> permeation through a lipid bilayer membrane composed of pure POPE (Fig. 3 *d*). Two barriers, one per leaflet, of  $\sim 4$  kJ/mol were observed at the intersection between the polar headgroups and the aliphatic chains of the lipids, indicating

hydrogen bonds with Arg-195. Note that frequent hydrogen bonds between water molecules and Arg-195 break upon CO<sub>2</sub> passage.

that the POPE membrane is highly permeable to CO<sub>2</sub>. As can be seen from Fig. 3 *d*, the free energy barrier coincides with an enthalpy minimum, rendering the free energy barrier either entropic or due to indirect, water-mediated enthalpic effects. A set of simulations in which CO<sub>2</sub> was allowed to diffuse freely corroborated the small barrier for CO<sub>2</sub> permeation across the POPE membrane. In 8 simulations of 11 ns each, 112 barrier crossings were observed in total for the 92 CO<sub>2</sub> molecules that were simulated. Inside the membrane, the CO<sub>2</sub> molecules diffused rapidly, i.e., the energetic barriers near the lipid headgroups limit the permeation through the bilayer. The permeability constant calculated from these simulations is  $P_f^{\text{POPE}} = 12 \text{ cm/s}$ .

This value is  $\sim 8$  times higher than the CO<sub>2</sub> permeability for artificial membranes reported by Prasad et al. (24). The discrepancy could be due to i), limitations of the force field used in the simulation; ii), the different lipid composition; and iii), remaining unstirred layer effects in experiments even at high concentrations of HCO<sub>3</sub><sup>-</sup> and carbonic anhydrase (CA). Given a membrane with intrinsic permeability  $P_f^M$ , surrounded by two unstirred layers of thickness  $d$  each, the total permeability  $P_f^{\text{tot}}$  obeys  $(P_f^{\text{tot}})^{-1} = (P_f^M)^{-1} + (D/2d)^{-1}$ .  $D$  denotes the diffusion constant of CO<sub>2</sub> in water,  $D/d$  can be considered as a permeability of a single unstirred layer. Outside the unstirred layers the CO<sub>2</sub> concentration is considered constant due to some buffer. Using this relation, a diffusion constant of  $2 \times 10^{-5} \text{ cm}^2/\text{s}$ , two unstirred layers of thickness 60 nm each and an intrinsic membrane permeability of 12 cm/s yields a total permeability of  $\sim 1.5 \text{ cm/s}$ , i.e., approximately the value reported by Prasad et al. for artificial membranes. The CA concentration of 0.5 mg/ml used by Prasad et al. refers to one CA enzyme per  $(45 \text{ nm})^3$ . Therefore, if CA is not bound to the membrane, the assumption that CO<sub>2</sub> needs to diffuse through a water layer of 60 nm before entering the membrane is within a realistic order of magnitude. This analysis implies that in experiments, CO<sub>2</sub> permeation through membranes with high intrinsic permeability like POPE might be limited by the diffusion of CO<sub>2</sub> from CA to the membrane and from the membrane to CA inside the liposome, even at high pH (or high HCO<sub>3</sub><sup>-</sup> concentration) and high CA concentration. Therefore, intrinsic membrane permeabilities might be underestimated by experiments under such conditions.

## CONCLUSIONS

Taken together, these results suggest that CO<sub>2</sub> permeation through AQP1 can be expected to play a physiological role only in membranes with a low intrinsic CO<sub>2</sub> permeability, such as membranes of cells exposed to an inhospitable environment (26,31). Membranes with similar physicochemical characteristics to POPE are highly permeable to CO<sub>2</sub>, rendering a physiological role for AQP1-mediated CO<sub>2</sub> permeation in such membranes unlikely. The role of AQP1 mediated CO<sub>2</sub> permeation in red blood cells, mammalian lungs and other

tissues therefore depends on the intrinsic CO<sub>2</sub> permeability of the surrounding membrane. Only for membranes with an activation barrier well above 20 kJ/mol or an empty central channel can AQP1-mediated CO<sub>2</sub> permeation be expected to play a major role, if a high enough expression level is provided. An interesting test of this hypothesis would be an evaluation of the CO<sub>2</sub> permeability of vesicles with different lipid composition and different levels of embedded AQP1.

We thank Gerrit Groenhof for calculation of the CO<sub>2</sub> partial charges and Helmut Grubmüller for critically reading the manuscript.

This project was supported by European Union grant No. LSHP-CT-2004-012189.

## REFERENCES

- Preston, G. M., T. P. Carroll, W. B. Guggino, and P. Agre. 1992. Appearance of water channels in *Xenopus* oocytes expressing red-cell CHIP28 protein. *Science*. 256:385–387.
- Zeidel, M. L., S. V. Ambudkar, B. L. Smith, and P. Agre. 1992. Reconstitution of functional water channels in liposomes containing purified red-cell CHIP28 protein. *Biochemistry*. 31:7436–7440.
- Maurel, C., J. Reizer, J. I. Schroeder, M. J. Chrispeels, and M. H. Saier. 1994. Functional characterization of the *Escherichia coli* glycerol facilitator, GlpF, in *Xenopus* oocytes. *J. Biol. Chem.* 269:11869–11872.
- Agre, P., M. Bonhivers, and M. J. Borgnia. 1998. The aquaporins, blueprints for cellular plumbing systems. *J. Biol. Chem.* 273:14659–14662.
- Deen, P. M. T., and C. H. van Os. 1998. Epithelial aquaporins. *Curr. Opin. Cell Biol.* 10:435–442.
- Nielsen, S., J. Frøkiær, D. Marples, T.-H. Kwon, P. Agre, and M. A. Knepper. 2002. Aquaporins in the kidney: From molecules to medicine. *Physiol. Rev.* 82:205–244.
- Kozono, D., M. Yasui, L. S. King, and P. Agre. 2002. Aquaporin water channels: atomic structure molecular dynamics meet clinical medicine. *J. Clin. Invest.* 109:1395–1399.
- King, L. S., D. Kozono, and P. Agre. 2004. From structure to disease: the evolving tale of aquaporin biology. *Nat. Rev. Mol. Cell Biol.* 5:687–698.
- Murata, K., K. Mitsuoka, T. Walz, P. Agre, J. Heymann, A. Engel, and Y. Fujiyoshi. 2000. Structural determinants of water permeation through Aquaporin-1. *Nature*. 407:599–605.
- Sui, H., B.-G. Han, J. K. Lee, P. Walian, and B. K. Jap. 2001. Structural basis of water-specific transport through the AQP1 water channel. *Nature*. 414:872–878.
- Savage, D. F., P. F. Egea, Y. Robles-Colmenares, J. D. O'Connell III, and R. M. Stroud. 2003. Architecture and selectivity in aquaporins: 2.5 Å x-ray structure of aquaporin Z. *PLoS Biol.* 1:e72.
- Gonen, T., P. Sliz, J. Kistler, Y. Cheng, and T. Walz. 2004. Aquaporin-0 membrane junctions reveal the structure of a closed water pore. *Nature*. 429:193–197.
- Harries, W. E. C., D. Akhavan, L. J. W. Miercke, S. Khademi, and R. M. Stroud. 2004. The channel architecture of aquaporin-0 at a 2.2-Å resolution. *Proc. Natl. Acad. Sci. USA*. 101:14045–14050.
- Fu, D., A. Libson, L. J. Miercke, C. Weitzman, P. Nollert, J. Krucinski, and R. M. Stroud. 2000. Structure of a glycerol-conducting channel and the basis for its selectivity. *Science*. 290:481–486.
- Stroud, R. M., D. Savage, L. J. W. Miercke, J. K. Lee, S. Khademi, and W. Harries. 2003. Selectivity and conductance among the glycerol and water conducting aquaporin family of channels. *FEBS Lett.* 555:79–82.
- de Groot, B. L., and H. Grubmüller. 2001. Water permeation across biological membranes: mechanism and dynamics of Aquaporin-1 and GlpF. *Science*. 294:2353–2357.

17. Tajkhorshid, E., P. Nollert, M. Ø. Jensen, L. J. W. Miercke, J. O'Connell, R. M. Stroud, and K. Schulten. 2002. Control of the selectivity of the aquaporin water channel family by global orientational tuning. *Science*. 296:525–530.
18. de Groot, B. L., T. Frigato, V. Helms, and H. Grubmüller. 2003. The mechanism of proton exclusion in the aquaporin-1 water channel. *J. Mol. Biol.* 333:279–293.
19. Chakrabarti, N., E. Tajkhorshid, B. Roux, and R. Pomes. 2004. Molecular basis of proton blockage in aquaporins. *Structure*. 12: 65–74.
20. Chakrabarti, N., B. Roux, and R. Pomes. 2004. Structural determinants of proton blockage in aquaporins. *J. Mol. Biol.* 343:493–510.
21. Ilan, B., E. Tajkhorshid, K. Schulten, and G. A. Voth. 2004. The mechanism of proton exclusion in aquaporin channels. *Proteins*. 55: 223–228.
22. Nakhoul, N. L., B. A. Davis, M. F. Romero, and W. F. Boron. 1998. Effect of expressing the water channel aquaporin-1 on the CO<sub>2</sub> permeability of *Xenopus* oocytes. *Am. J. Physiol. Cell Physiol.* 274: C543–C548.
23. Cooper, G. J., and W. F. Boron. 1998. Effect of PCMBs on CO<sub>2</sub> permeability of *Xenopus* oocytes expressing aquaporin 1 or its C189S mutant. *Am. J. Physiol.* 275:C1481–C1486.
24. Prasad, G. V. R., L. A. Coury, F. Finn, and M. L. Zeidel. 1998. Reconstituted aquaporin-1 water channels transport CO<sub>2</sub> across membranes. *J. Biol. Chem.* 273:33123–33126.
25. Yang, B., N. Fukuda, A. van Hoek, M. A. Matthey, T. Ma, and A. S. Verkman. 2000. Carbon dioxide permeability of aquaporin-1 measured in erythrocytes and lung of aquaporin-1 null mice and in reconstituted proteoliposomes. *J. Biol. Chem.* 275:2686–2692.
26. Cooper, G. J., Y. Zhou, P. Bouyer, I. I. Grichtchenko, and W. F. Boron. 2002. Transport of volatile solutes through AQP1. *J. Physiol.* 542: 17–29.
27. Verkman, A. S. 2002. Does aquaporin-1 pass gas? An opposing view. *J. Physiol.* 542:31.
28. Fang, X., B. Yang, M. A. Matthey, and A. S. Verkman. 2002. Evidence against aquaporin-1-dependent CO<sub>2</sub> permeability in lung and kidney. *J. Physiol.* 542:63–69.
29. Blank, M. E., and H. Ehmke. 2003. Aquaporin-1 and HCO<sub>3</sub><sup>-</sup>-Cl<sup>-</sup> transporter-mediated transport of CO<sub>2</sub> across the human erythrocyte membrane. *J. Physiol.* 550.2:419–429.
30. Gutknecht, J., M. A. Bisson, and F. C. Tosteson. 1977. Diffusion of carbon dioxide through lipid bilayer membranes: effects of carbonic anhydrase, bicarbonate, and unstirred layers. *J. Gen. Physiol.* 69:779–794.
31. Waisbren, S. J., J. P. Geibel, I. M. Modlin, and W. F. Boron. 1994. Unusual permeability properties of gastric gland cells. *Nature*. 368: 332–335.
32. Uehlein, N., C. Lovisollo, F. Siefert, and R. Kaldenhoff. 2003. The tobacco aquaporin NtAQP1 is a membrane CO<sub>2</sub> pore with physiological functions. *Nature*. 425:734–737.
33. Vriend, G. 1990. WHAT IF: a molecular modeling and drug design program. *J. Mol. Graph.* 8:52–56.
34. Jorgensen, W. L., J. Chandrasekhar, J. D. Madura, R. W. Impney, and M. L. Klein. 1983. Comparison of simple potential functions for simulating liquid water. *J. Chem. Phys.* 79:926–935.
35. Jorgensen, W. L., D. S. Maxwell, and J. Tirado-Rives. 1996. Development and testing of the OPLS all-atom force field on conformational energetics and properties of organic liquids. *J. Am. Chem. Soc.* 118:11225–11236.
36. Kaminski, G. A., R. A. Friesner, J. Tirado-Rives, and W. L. Jorgensen. 2001. Evaluation and reparametrization of the OPLS-AA force field for proteins via comparison with accurate quantum chemical calculations on peptides. *J. Phys. Chem. B*. 105:6474–6487.
37. Berger, O., O. Edholm, and F. Jähnig. 1997. Molecular dynamics simulations of a fluid bilayer of dipalmitoylphosphatidylcholine at full hydration, constant pressure, and constant temperature. *Biophys. J.* 72:2002–2013.
38. Lindahl, E., B. Hess, and D. Van der Spoel. 2001. GROMACS 3.0: a package for molecular simulation and trajectory analysis. *J. Mol. Model. (Online)*. 7:306–317 (Internet).
39. Van der Spoel, D., E. Lindahl, B. Hess, G. Groenhof, A. E. Mark, and H. J. C. Berendsen. 2005. GROMACS: Fast, flexible and free. *J. Comput. Chem.* 26:1701–1718.
40. Darden, T., D. York, and L. Pedersen. 1993. Particle mesh Ewald: an N·log(N) method for Ewald sums in large systems. *J. Chem. Phys.* 98: 10089–10092.
41. Essmann, U., L. Perera, M. L. Berkowitz, T. Darden, H. Lee, and L. G. Pedersen. 1995. A smooth particle mesh Ewald potential. *J. Chem. Phys.* 103:8577–8592.
42. Miyamoto, S., and P. A. Kollman. 1992. SETTLE: An analytical version of the SHAKE and RATTLE algorithms for rigid water models. *J. Comput. Chem.* 13:952–962.
43. Hess, B., H. Bekker, H. J. C. Berendsen, and J. G. E. M. Fraaije. 1997. LINCS: a linear constraint solver for molecular simulations. *J. Comput. Chem.* 18:1463–1472.
44. Berendsen, H. J. C., J. P. M. Postma, A. DiNola, and J. R. Haak. 1984. Molecular dynamics with coupling to an external bath. *J. Chem. Phys.* 81:3684–3690.
45. Jensen, M. Ø., and O. G. Mouritsen. 2006. Single-channel water permeabilities of *E. coli* aquaporins AqpZ and GlpF. *Biophys. J.* 90:2270–2284.
46. Kumar, S., D. Bouzida, R. H. Swendsen, P. A. Kollman, and J. M. Rosenberg. 1992. The weighted histogram analysis method for free-energy calculations on biomolecules. I. The method. *J. Comput. Chem.* 13:1011–1021.
47. Forster, R. E., G. Gros, L. Lin, Y. Ono, and M. Wunder. 1998. The effect of 4,4'-diisothiocyanato-stilbene-2,2'-disulfonate on CO<sub>2</sub> permeability of the red blood cell membrane. *Proc. Natl. Acad. Sci. USA*. 95:15815–15820.
48. Walz, T., B. L. Smith, M. L. Zeidel, A. Engel, and P. Agre. 1994. Biologically active two-dimensional crystals of aquaporin CHIP. *J. Biol. Chem.* 269:1583–1586.
49. Jiang, J., B. V. Daniels, and D. Fu. 2006. Crystal structure of aquaporin Z tetramer reveals both open and closed water-conducting channels. *J. Biol. Chem.* 281:454–460.
50. DeLano, W. L. 2002. The PyMOL Molecular Graphics System. <http://www.pymol.org>.